

# Wavefront measurements of phase plates combining a point-diffraction interferometer and a Hartmann–Shack sensor

Juan M. Bueno,<sup>1,\*</sup> Eva Acosta,<sup>2</sup> Christina Schwarz,<sup>1</sup> and Pablo Artal<sup>1</sup>

<sup>1</sup>Laboratorio de Óptica, Centro de Investigación en Óptica y Nanofísica (CiOyN),  
Universidad de Murcia, Campus de Espinardo, 30100 Murcia, Spain

<sup>2</sup>Área de Óptica, Facultad de Física, Universidad de Santiago de Compostela,  
15782 Santiago de Compostela, Spain

\*Corresponding author: bueno@um.es

Received 3 November 2009; revised 14 December 2009; accepted 14 December 2009;  
posted 15 December 2009 (Doc. ID 119451); published 15 January 2010

A dual setup composed of a point diffraction interferometer (PDI) and a Hartmann–Shack (HS) wavefront sensor was built to compare the estimates of wavefront aberrations provided by the two different and complementary techniques when applied to different phase plates. Results show that under the same experimental and fitting conditions both techniques provide similar information concerning the wavefront aberration map. When taking into account all Zernike terms up to 6th order, the maximum difference in root-mean-square wavefront error was  $0.08\ \mu\text{m}$ , and this reduced up to  $0.03\ \mu\text{m}$  when excluding lower-order terms. The effects of the pupil size and the order of the Zernike expansion used to reconstruct the wavefront were evaluated. The combination of the two techniques can accurately measure complicated phase profiles, combining the robustness of the HS and the higher resolution and dynamic range of the PDI. © 2010 Optical Society of America

OCIS codes: 080.1010, 120.3180, 120.4630, 130.6010.

## 1. Introduction

For many years there has been a special interest in measuring the quality of optical systems [1,2]. Although a large number of techniques are available for optical testing, interferometry [3] and wavefront sensing techniques [4–7] have been used extensively. The former include interferometric methods such as Michelson, Fizeau, Mach–Zehnder, point-diffraction and shearing, and holographic techniques, among others. Examples of the latter ones are the Foucault knife-edge test, curvature or Hartmann–Shack (HS) sensors, etc. Despite the different nature of both types of technique, the wavefront aberration (WA) of the beam emerging from the system can be reconstructed to estimate the optical quality.

In particular, our interest in this study is to compare the estimations of the WAs from two different, and somehow complementary, techniques: a point-diffraction interferometer (PDI) and a HS wavefront sensor. To our best knowledge their equivalence has not previously been reported. This would establish which is best suited for a particular experimental situation, or more interestingly, when the combination of the two would provide the best results. Although originally designed to be used in astronomy [8], during the past few years HS sensors have successfully been used in exploring ocular aberrations [9–12]. On the other hand, the PDI is not a tool as extended in the analysis of ocular aberrations as the HS, although it has also been used in astronomy [13,14] and optical testing [15,16].

The PDI is a simple common-path interferometer used to directly measure optical-path differences [14–17]. The technique is based on the interference

---

0003-6935/10/030450-07\$15.00/0  
© 2010 Optical Society of America

between a reference spherical beam generated by diffraction through a clear, small pinhole in a semitransparent plate and the beam under test focused in the vicinity of the pinhole. On the other hand, with a HS sensor [8] the wavefront is sampled by a microlens array in such a way that each sampled light pencil is brought to a particular location in the focal plane. If the wavefront is aberrated, these spots shift from the regularly spaced ideal spot pattern produced by a plane wavefront. These displacements provide information on the local slope of the wavefront over each microlens, and then the WA can be reconstructed.

## 2. Methods

### A. Experimental System

A custom dual setup combining a PDI and a HS sensor has been developed. A schematic diagram (lateral view) is shown in Fig. 1. The light source is a 633 nm He-Ne laser that was collimated before reaching the beam splitter (BS). The transmitted and reflected portions of the beam are used for the PDI and HS measurements, respectively.

In the HS arm the light passes a neutral density filter (NDF) used to reduce the intensity and an aperture, AP1, that controls the beam size to fit the sample under test. The beam then passes the sample, is reflected in a mirror (M1), and is transmitted through a telescope composed of two lenses (L1 and L2) that makes the sample's plane optically conjugated with the HS microlens (ML) array. This telescope provides a 0.75 magnification to optically relay the spot's image onto the HS-CCD plane. The ML array has a focal length of 3.7 mm and a microlens pitch of 0.146 mm. Before image registration, every sample was centered with respect to the incident beam. The WA of the sample in transmission is reconstructed from the HS images as previously reported [18]. Briefly, when a plane wavefront reaches the ML, the image recorded by the CCD is a set of spots distributed in a perfectly regular pattern, but if the wavefront is aberrated (i.e., distorted), this pattern becomes irregular. Each spot moves in such a way that the displacements in the  $x$  and  $y$  directions are proportional to the partial derivatives of the wavefront averaged over each microlens area. From

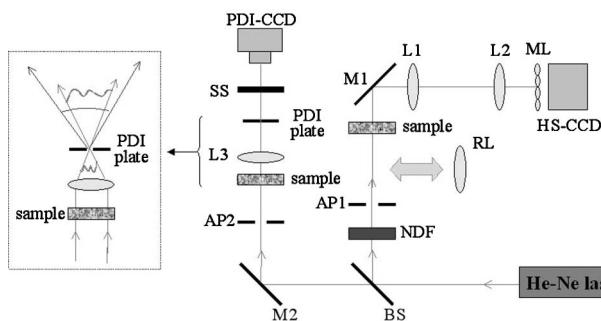


Fig. 1. Simplified schematic diagram of the experimental dual setup PDI-HS (see text for details). Inset: detail of the PDI interferometer with the PDI plate in focus.

each HS image, shown in Fig. 2(a), the WA of the sample under test, Fig. 2(b), is calculated and expressed as a Zernike polynomial expansion.

The beam transmitted by the BS travels along the PDI pathway (left part of Fig. 1). As explained above, the principle of this technique is the interference between a reference spherical beam generated by diffraction through a clear pinhole placed in a semitransparent plate (PDI plate) and the beam under test focusing in the vicinities of the pinhole (inset in Fig. 1; see [15,17] for further details). Similar to the HS sensor, the PDI was built to measure the WA of different samples in transmission. All the samples were under the same alignment conditions as in the HS. The collimated beam, limited in size by AP2, illuminates the sample. Since our particular samples are nominally flat (see Subsection 2.B), a lens (L3) is required to make the beam convergent to the PDI plate. The used PDI plate is a silica substrate coated with chromium oxide with an optical density of 2.3 and pinhole diameter of  $7\ \mu\text{m}$ , which was mounted on an XYZ translation stage. The interferogram is projected on a semitransparent screen (SS) optically conjugated with the PDI-CCD camera [Fig. 3(a)]. For each interferogram, dark fringes are semiautomatically tracked [Fig. 3(b)]. These fringes represent isophase curves in such a way that the separation between two consecutive curves equals one  $\lambda$ . From the phase values of the curves at each  $(x,y)$  location, the phase map is reconstructed [Fig. 3(c)] and fitted to a Zernike polynomial series. In order to have the same experimental conditions only one interferogram without carrier fringes was taken for this experiment. In both techniques, depending on the samples used here (see the results, Section 3), different pupil sizes (7 and 4 mm) and Zernike expansion orders (6th, 5th, or 4th) were used. The root-mean-square (RMS) wavefront error will be used as an image quality parameter.

### B. Samples Used

The main goal of this work was to test the results of WAs obtained with the two methods described above. For this aim we required samples providing well-known WA patterns. In particular we used two custom phase plates. Phase plate #1 has Zernike

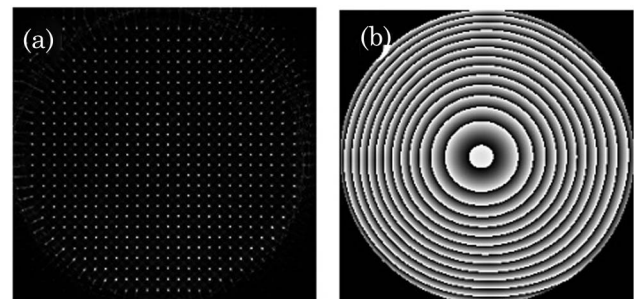


Fig. 2. Examples of (a) a typical HS spot pattern and (b) the corresponding computed WA including Zernike terms from the 2nd to the 6th orders.

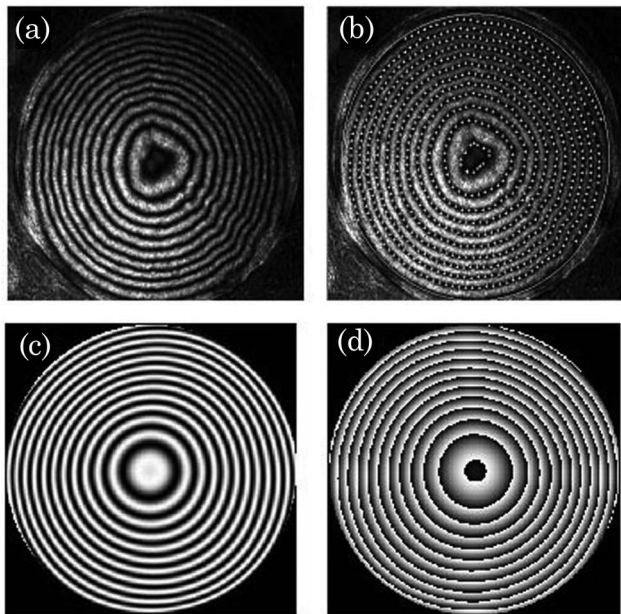


Fig. 3. (a) Example of a PDI interferogram, (b) isophase curve tracking for image analysis, (c) reconstructed interferogram, (d) WA map.

coefficients  $Z_3^3$  and  $Z_5^3$  (3rd- and 5th-order trefoil terms) as dominant, and phase plate #2 contained a mix of different Zernike terms, defocus ( $Z_2^0$ ) and spherical aberration ( $Z_4^0$ ) being the dominant ones. Zernike coefficients  $Z_2^0$ ,  $Z_3^3$ ,  $Z_4^0$ , and  $Z_5^3$  correspond to terms 5, 10, 13, and 20. The effective phase plate diameters were 7 mm for plate #1 and 4 mm for plate #2. The plates were manufactured using a gray-level single-mask photosculpture in photoresist technique [19]. Figure 4 presents the interferograms registered with a Mach-Zehnder interferometer provided by the manufacturer.

For completeness and for later comparisons, the corresponding real far-field point spread function (PSF) for each plate was registered with an auxiliary experimental system [Fig. 5(a)]. This used a collimated laser beam to illuminate the phase plate. The PSF was directly registered with a CCD camera that was optically conjugated with the phase plate plane through an objective. These PSFs are shown in Figs. 5(b) and 5(c).

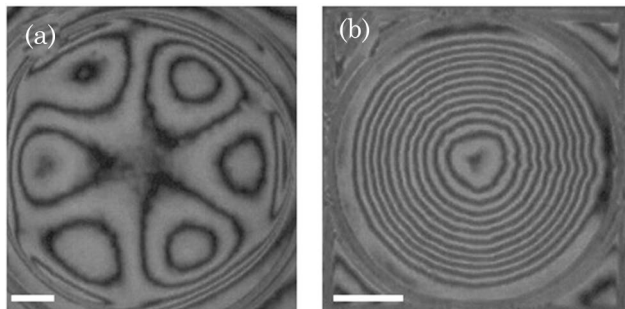


Fig. 4. Measured interferograms of phase plates (a) #1 and (b) #2 provided by the manufacturer. These were registered with a Mach-Zehnder interferometer. Bars are 1 mm long.

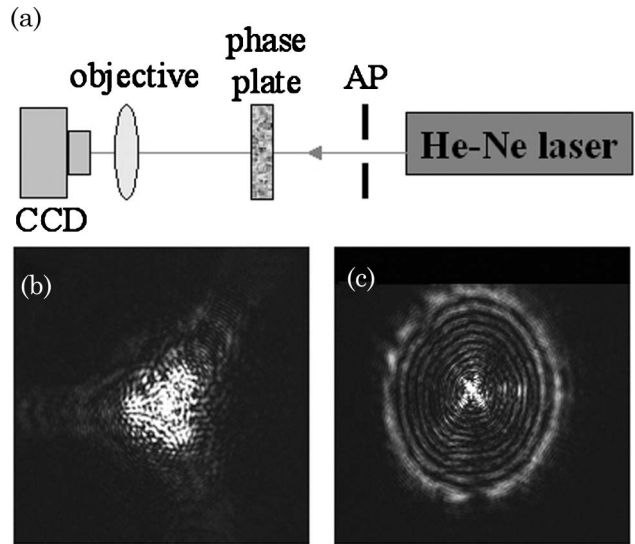


Fig. 5. (a) Layout of the auxiliary experimental system used to register the far-field PSF; real far-field PSFs for phase plate (b) #1 and (c) #2.

### 3. Results

#### A. Sample #1

Figure 6(a) shows the interferogram taken with the PDI for phase plate #1. This is similar to that in Fig. 4(a) given by the manufacturer and registered with a different type of interferometer. Figures 6(b) and 6(d) present the WAs (from 2nd- to 6th-order but defocus) computed from the HS and PDI images for a 7 mm pupil. The associated PSFs [Figs. 6(c) and 6(e)] are also shown. A visual inspection shows that the WAs provided by both techniques look similar.

The WAs and the PSFs obtained from both wavefront sensing and interferometry agree well with the information provided by the manufacturer (Fig. 4). Figure 7 presents the individual Zernike coefficients up to 5th order (after fitting up to 6th order). The values of 6th-order terms have little influence in

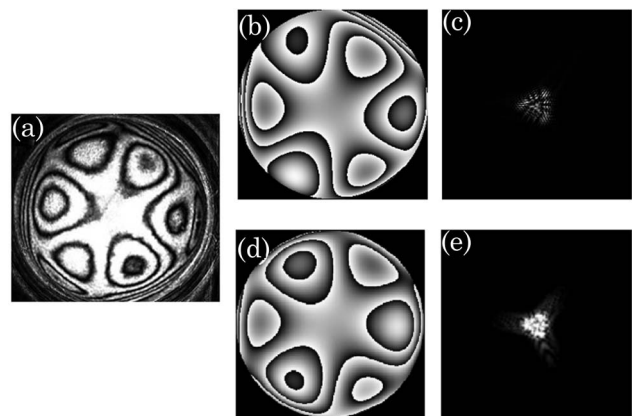


Fig. 6. (a) Interferogram registered with the PDI for plate #1. (b) WAs ( $2\pi$ -phase wrapped) including Zernike terms from 2nd to 6th orders but defocus, computed from (b) HS and (d) PDI images corresponding to phase plate #1. The associated PSFs for the (c) HS and (e) the PDI are shown in the right column.

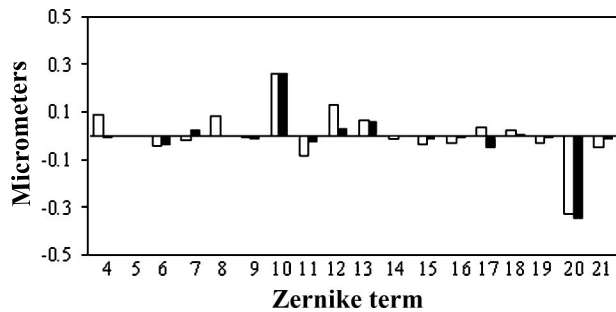


Fig. 7. Individual Zernike coefficient values of the WA (up to 5th order) for phase plate #1 computed from HS (white bars) and PDI (black bars) measurements. The order of the terms corresponds to the OSA notation.

the total WA, with RMS values of 0.08 and 0.03  $\mu\text{m}$  for the HS and PDI technique, respectively.

The comparison shows that both techniques provide similar results. In particular, the corresponding RMS values (from 2nd to 6th order excluding defocus) were 0.48 and 0.45  $\mu\text{m}$  for the HS and PDI technique, respectively. As expected, the individual Zernike terms with larger values correspond to  $Z_5^3$  (term 20) and  $Z_3^3$  (term 10), both trefoil terms. The values of these particular aberrations match well (Fig. 8). Moreover, the RMS values corresponding to 5th order were 0.34 and 0.35  $\mu\text{m}$  for HS sensing and interferometry, respectively, and 0.27 and 0.26  $\mu\text{m}$  for 3rd-order terms.

In view of these contributions from the different orders, we analyzed again the images provided by both techniques using Zernike expansions up to 6th (Fig. 6), 5th, and 4th orders. Figure 9 shows the computed WAs for 5th and 4th orders. The former are very similar to those in Fig. 6, however when the expansion is truncated to 4th order, the WAs change significantly, although both techniques present once again similar results, thus showing that undermodeling yields to erroneous determination of the WAs.

For a better understanding and as an example, Fig. 10 presents the individual Zernike terms for expansions up to 5th and 4th order obtained from HS measurements. Similar behavior was found for PDI data.

Since the effective size of plate #1 is 7 mm, we also tested the influence of reducing the pupil size. Then,

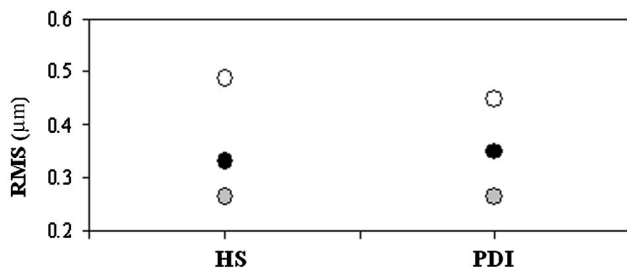


Fig. 8. Comparison of contributions of different Zernike terms between HS and PDI techniques for phase plate #1. RMS values for all terms but defocus (white symbols); values of terms 10 (gray symbols) and 20 (black symbols).

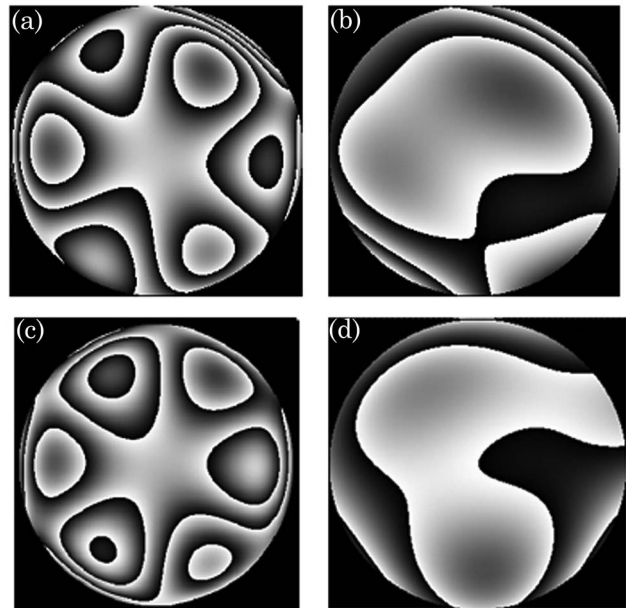


Fig. 9. WAs computed from the HS (a), (b) and PDI (c), (d) images using the Zernike expansion up to 5th (a), (c) and 4th (b), (d) order. Defocus was always excluded.

we kept the order of the Zernike expansion, but the analyzed pupil size changed from 7 to 4 mm. Figure 11 presents the WAs expanded up to 6th order (no defocus) across a 4 mm pupil for both techniques. Once again, both techniques show similar WA maps, however they are very different from those computed for a 7 mm pupil (Fig. 6). This fact can be better observed in Fig. 12 for the HS measurements. This figure plots the individual Zernike terms for both pupil sizes. Results were similar for PDI.

The information on term 20 (mode  $Z_5^3$ ) is mainly located in the vicinity of the edges of the phase plate. Thus when reducing the pupil size, the information on this mode disappears, and it is transferred to mode  $Z_3^3$  (term 10). However this does not necessarily provide the wrong phase values in the central region of the plate under measurement. Moreover, in both techniques, noise as well as the uncertainty in the measurements: location of centroids in the HS images and tracking of the equiphase fringes in the PDI make the least-squares solution limit

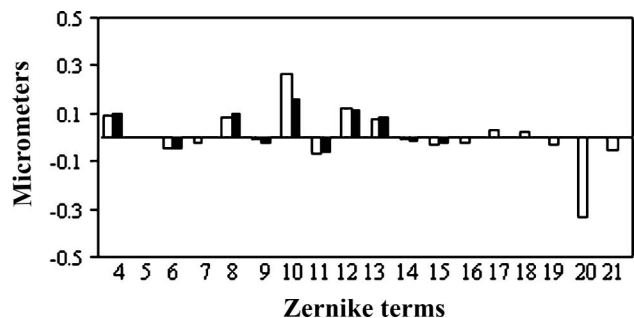


Fig. 10. Zernike coefficients from HS measurement for phase plate #1 computed up to 5th (white bars) and 4th (black bars) orders.

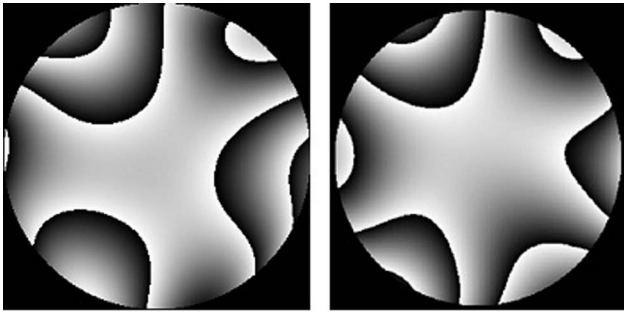


Fig. 11. Effect of reducing the pupil size from 7 mm (Fig. 6) to 4 mm on plate #1. WA results from HS (left) and PDI (right) measurements.

the accuracy of the phase map reconstruction especially in higher-order modes.

### B. Sample #2

Phase plate #2 was measured with the same experimental conditions as plate #1 and the pupil size used was 4 mm. The WAs from 2nd to 6th order for this plate are those depicted in Figs. 2(b) (from HS) and 3(d) (from PDI). It can be observed that both present small differences and that defocus is the dominant term. This fact is better shown in Fig. 13, which includes the Zernike coefficients up to 5th order for both techniques as well as the corresponding PSFs.

Total RMS values were, respectively, 2.09 and 2.01  $\mu\text{m}$  for HS and PDI measurements. If defocus is excluded, the RMS values were, respectively, 0.24 and 0.22  $\mu\text{m}$ , which corroborates the dominance of this term. For a better understanding, Fig. 14 presents the WAs obtained with both methods when eliminating the contribution of defocus. As a comparison, the real PDI image without defocus is also included. This image was obtained by axially moving the pinhole, which is equivalent to introducing circular carrier fringes or compensating for defocus.

The influence of the different orders is depicted in Fig. 15 for HS images. This shows the WAs (excluding defocus) obtained when using expansions up to 6th, 5th, and 4th orders. It can be observed that WAs are similar, which indicates the small influence of higher-order aberrations for this plate #2. When processing the images up to 5th order, RMS values

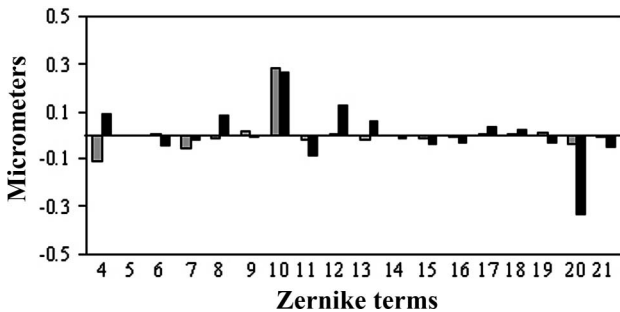


Fig. 12. Zernike coefficient values for phase plate #1 computed from HS for 4 (gray bars) and 7 mm (black bars) pupil. Data for 7 mm are the same as those presented in Fig. 7.

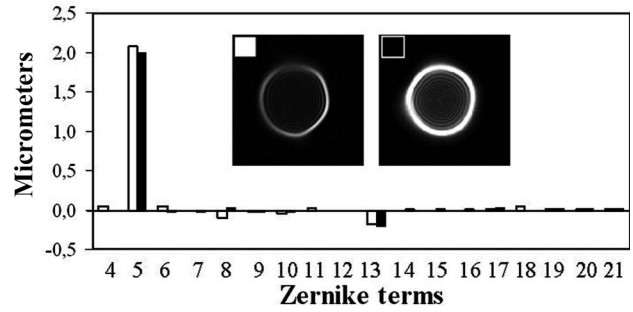


Fig. 13. Individual Zernike coefficients for the WA of phase plate #2 computed from HS (white bars) and PDI (black bars) images and a 4 mm pupil. Insets are the corresponding far-field PSFs.

were 0.23  $\mu\text{m}$  for HS (Fig. 15, middle) and 0.22  $\mu\text{m}$  for PDI. These values are 0.21 and 0.22  $\mu\text{m}$ , respectively, when the Zernike series is expanded up to 4th order. This means that for this phase plate #2 the contribution of 6th and 5th orders has little significance. In fact all high-order Zernike terms were smaller than 0.04  $\mu\text{m}$ , but spherical aberration ( $Z_4^0 \sim 0.19 \mu\text{m}$ ) and trefoil ( $Z_3^3 \sim 0.05 \mu\text{m}$ ). In both techniques the small distortions of the fringes [see Fig. 3(a), where equi-phase curves are slightly distorted in some regions, these distortions being around  $\lambda/10$ ] are softened due not only to the finite sampling but also to the polynomial fit.

### 4. Discussion

We have presented an experimental system combining two complementary, although conceptually different, techniques: a PDI and HS wavefront sensor. The experimental procedure was validated by measuring calibrated flat phase plates with known aberrations under the same experimental conditions, illuminated with a monochromatic collimated laser beam. Results of WAs obtained from both techniques have been qualitatively and quantitatively compared.

The two experimental methods are operationally different, and each one presents advantages and disadvantages. In particular, a PDI is a very simple and efficient technique used in differing applications such as optical testing, lithography, and gas-phase temperature measurements, among others [16,20]. In a PDI, the interference pattern is thus equivalent to the interference between the actual wave and a spherical reference wave generated by the pinhole. Therefore, the interference pattern can be easily

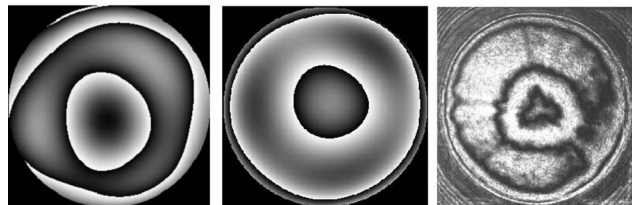


Fig. 14. WAs computed from the HS image (left) and the PDI interferogram (middle) using the Zernike expansion up to 6th order and excluding defocus. Corresponding real "in focus" PDI interferogram (is shown at the right).

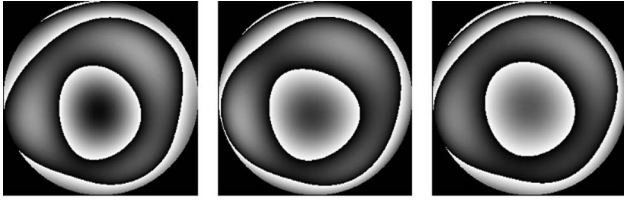


Fig. 15. WAs (defocus excluded) computed from the HS images using the Zernike expansion up 6th (left), 5th (middle), and 4th (right) orders. Defocus was always included.

interpreted as the phase aberration of the wave, plus some small amount of defocus and tilt in case the pinhole is not placed at focus. The possibility of placing the pinhole slightly out of focus implies that circular carrier fringes and/or linear carrier fringes can be easily introduced and controlled. This technique permits the direct visualization of the constant phase fringes and therefore a simple visual analysis of the recorded interferogram. However, the computation of the actual WA requires postprocessing of the images from manual tracking of dark fringes, with the accuracy limitations that a manual process implies. However from an interferometric point of view the PDI is an attractive device since it uses a single optical element, it is not sensitive to vibration (common-path design), and it can directly measure optical path differences. Moreover, the use of a PDI pinhole of about a few micrometers not only facilitates the alignment but also increases the dynamic range of the interferometer, allowing one to measure highly aberrated samples (although at the expense of losing contrast of the fringes at some regions near the periphery, which can be compensated by joint analysis of several interferograms under different carrier fringes). Nevertheless, as the location of the regions with low contrast depends on the position of the pinhole (i.e., the amount of circular and linear carrier fringes), the aberration in all the region of interest can be obtained by joint processing of several interferograms differing only in the amount of circular and linear carrier fringes.

It must be pointed out that PDI allows us to visualize regions with phase dislocations or without fringe continuity (that is, regions where Y or 8-shaped fringes are present), or with no phase derivability (i.e., where fringes are continuous but not smooth). If phase dislocations occur, circular and linear carrier fringes together with the proper algorithm allow for the evaluation of the interferogram. Then PDI can measure discontinuous surfaces as long as you can keep track of the  $2\pi$  phase ambiguity.

The main disadvantage of a PDI is the lost light due to the absorption of the plate's semitransparent coating (optical density of about 2.3) needed to match the intensity of the beam under test passing the plate and the intensity of the reference wave created by the pinhole (in order to have high contrast fringes). Therefore for those applications with low light levels where long integration times are not allowed, PDI is not a good choice. It is also worthwhile to mention

that in applications requiring a high degree of accuracy ( $\lambda/200$  or smaller) the use of a transmission diffraction grating and a plate with two pinholes adds a phase shifting capability able to improve the performance of the system [21].

On the other hand, the HS wavefront sensor does not require coherent light and is used widely in astronomical, ocular, and general optical testing applications, including control of the aberrations of a high-power laser system [22]. Unlike the PDI, from the HS image itself, no relevant information can be obtained, however the analysis to obtain the WA can be done in real time. This real time monitoring allows easy experimental alignment, even for biological samples with more irregular aberration patterns. The dynamic range of the HS is determined by the spatial resolution and the focal length of the microlens array. Since details smaller than the microlens size cannot be captured, a limited spatial resolution might produce a smoother WA, leading to the loss of some details and image quality overestimation of some highly aberrated areas. In addition, spot overlapping might be a result of a long focal length, producing wrong estimates of the WA. In the present experiment, the parameters of the microlens array and the size of the PDI pinhole are appropriate to obtain accurate results.

Despite advantages and disadvantages, as well as differences between the two techniques, the results for WAs obtained with both the PDI and the HS sensor are comparable. A visual inspection of both WAs and PSFs indicates a good agreement. The WAs are also coherent with the information provided by the manufacturer (Fig. 4). Moreover, the PSFs experimentally measured (Fig. 5) can also be qualitative compared with those computed from the WAs (Figs. 6 and 13).

Within a quantitative comparison (Figs. 7, 8, and 13), there was also a close match between the dominant Zernike terms for the two phase plates. The RMS wavefront error values for the different orders also agree, the maximum difference being  $0.09 \mu\text{m}$ . We have also tested the influence of reducing the pupil size (plate #1) and the order of the Zernike expansion (plates #1 and #2). Once again, we found a close agreement between the PDI and the HS,  $0.10 \mu\text{m}$  being the highest difference in RMS (corresponding to plate #1, 4 mm pupil and 4th-order Zernike expansion). Overall, the RMS error between techniques taking into account all individual Zernike coefficients up to 6th order was below  $\lambda/3$ .

Throughout this paper we have used nominally flat phase objects, however, if the phase object to be tested is a focusing element the experimental configuration must be changed and an additional lens must be added into the beam pathway. Under these circumstances the laser beam would enter the sample differently in the PDI and in the HS sensor, this might lead to individual differences that need to be explored in more depth. Although both techniques

have been used in visible light, its implementation with infrared light will be straightforward.

## 5. Conclusion

We have demonstrated the equivalence of two different and complementary techniques (a PDI and a HS sensor) for measuring the WAs of phase plates under the same experimental conditions. Despite the noticeable differences between instruments, the results provide the same information within the experimental error. In different applications, the combined use of both techniques, PDI and HS, could offer the optimum solution, by merging high resolution from the PDI with the more robust HS.

This research was supported by the Ministerio de Educación y Ciencia of Spain, grants FIS2007-63123 and FIS2007-64765; CONSOLIDER-INGENIO 2010, grant CSD2007-00033 SAUUL; and Fundación Seneca de la Región de Murcia, Spain, grant 4524/GERM/06. The authors thank Silvestre Manzanera for help recording the PSFs.

## References

1. D. Malacara, *Optical Shop Testing*, 2nd ed. (Wiley-Interscience, 1992).
2. J. M. Geary, *Introduction to Optical Testing* (SPIE Press, 1993).
3. J. C. Wyant, *Field Guide to Interferometric Optical Testing*, Vol. FG10 of SPIE Field Guide Series, E. P. Goodwin, ed. (SPIE Press, 2006).
4. D. R. Neal, D. J. Armstrong, and W. T. Turner, "Wavefront sensors for control and process monitoring in optics manufacture," *Proc. SPIE* **2993**, 211–220 (1997).
5. J. E. Greivenkamp, D. G. Smith, R. O. Gappinger, and G. A. Williby, "Optical testing using Shack-Hartmann wavefront sensors," *Proc. SPIE* **4416**, 260–263 (2001).
6. W. Jiang, X. Rao, Z. Yang, and N. Ling, "Applications of Hartmann-Shack wavefront sensors," *Proc. SPIE* **6018**, 192–200 (2005).
7. W. Zou and J. Rolland, "Differential wavefront curvature sensor," *Proc. SPIE* **5869**, 306–313 (2005).
8. G. Rousset, "Wavefront sensing," in *Adaptive Optics for Astronomy*, D. M. Alloin and J.-M. Mariotti, eds. (Kluwer Academic, 1994).
9. J. Liang, B. Grimm, S. Goelz, and J. F. Bille, "Objective measurement of wave aberrations of the human eye with the use of a Hartmann-Shack wave-front sensor," *J. Opt. Soc. Am. A* **11**, 1949–1957 (1994).
10. H. Hofer, P. Artal, B. Singer, J. L. Aragón, and D. R. Williams, "Dynamics of the eye's wave aberration," *J. Opt. Soc. Am. A* **18**, 497–506 (2001).
11. P. Artal, A. Guirao, E. Berrio, and D. R. Williams, "Compensation of corneal aberrations by internal optics in the human eye," *J. Vision* **1**, 1–8 (2001).
12. I. Brunette, J. M. Bueno, M. Harissi-Dagher, M. Parent, M. Podtetenov, and H. Hamam, "Optical quality of the eye with the artisan phakic lens for the correction of high myopia," *Optom. Vis. Sci.* **80**, 167–174 (2003).
13. R. N. Smartt and W. H. Steel, "Theory and application of point diffraction interferometers," *Jpn. J. Appl. Phys.* **14**, 351–356 (1975).
14. C. Koliopoulos, O. Kwon, R. Shagam, J. C. Wyant, and C. R. Hayslett, "Infrared point-diffraction interferometer," *Opt. Lett.* **3**, 118–120 (1978).
15. E. Acosta, S. Chamadoira, and R. Blendowske, "Modified point diffraction interferometer for inspection and evaluation of ophthalmic components," *J. Opt. Soc. Am. A* **23**, 632–637 (2006).
16. E. Tejnil, K. A. Goldberg, S. H. Lee, H. Medeck, P. J. Batson, P. E. Denham, A. A. MacDowel, and J. Bokor, "At wavelength interferometry for extreme ultraviolet lithography," *J. Vac. Sci. Technol. B* **15**, 2455–2461 (1997).
17. E. Acosta, D. Vázquez, and L. Rodríguez Castillo, "Analysis of the optical properties of crystalline lenses by point diffraction interferometry," *Optical. Physiol. Opt.* **29**, 235–246 (2009).
18. P. M. Prieto, F. Vargas-Martín, S. Goelz, and P. Artal, "Analysis of the performance of the Hartmann—Shack sensor in the human eye," *J. Opt. Soc. Am. A* **17**, 1388–1398 (2000).
19. R. Navarro, E. Moreno-Barriuso, S. Bará, and T. Mancebo, "Phase plates for wave-aberration compensation in the human eye," *Opt. Lett.* **25**, 236–238 (2000).
20. J. S. Goldmeer, D. L. Urban, and Z. Yuan, "Measurement of gas-phase temperatures in flames with a point diffraction interferometer," *Appl. Opt.* **40**, 4816–4823 (2001).
21. H. Medeck, E. Tejnil, K. A. Goldberg, and J. Bokor, "Phase shifting point diffraction interferometer," *Opt. Lett.* **21**, 1526–1528 (1996).
22. J. M. Bueno, B. Vohnsen, L. Roso, and P. Artal, "Temporal wavefront stability of an ultrafast high-power laser beam," *Appl. Opt.* **48**, 770–777 (2009).